Contents lists available at ScienceDirect

Engineering

journal homepage: www.elsevier.com/locate/eng

Research
Green Chemical Engineering—Article

Ce-Doped Smart Adsorbents with Photoresponsive Molecular Switches for Selective Adsorption and Efficient Desorption

Peng Tan, Yao Jiang, Shi-Chao Qi, Xia-Jun Gao, Xiao-Qin Liu *, Lin-Bing Sun *

State Key Laboratory of Materials-Oriented Chemical Engineering, Jiangsu National Synergetic Innovation Center for Advanced Materials, College of Chemical Engineering, Nanjing Tech University, Nanjing 211816, China

A B S T R A C T

Achieving efficient adsorption and desorption processes by controllably tuning the properties of adsorbents at different technical stages is extremely attractive. However, it is difficult for traditional adsorbents to reach the target because of their fixed active sites. Herein, we report on the fabrication of a smart adsorbent, which was achieved by introducing photoresponsive azobenzene derivatives with *cis/trans* isomers to Ce-doped mesoporous silica. These photoresponsive groups serve as "molecular switches" by sheltering and exposing active sites, leading to efficient adsorption and desorption. Ce is also doped to provide additional active sites in order to enhance the adsorption performance. The results show that the *cis* isomers effectively shelter the active sites, leading to the selective adsorption of methylene blue (MB) over brilliant blue (BB), while the *trans* isomers completely expose the active sites, resulting in the convenient release of the adsorbates. Both selective adsorption and efficient desorption can be realized controllably by these smart adsorbents through photostimulation. Moreover, the performance of the obtained materials is well maintained after five cycles.

© 2020 THE AUTHORS. Published by Elsevier LTD on behalf of Chinese Academy of Engineering and Higher Education Press Limited Company. This is an open access article under the CC BY-NC-ND license (http://creativecommons.org/licenses/by-nc-nd/4.0/).

1. Introduction

Adsorptive separation utilizing solid adsorbents has attracted increasing attention in the past decades due to the low equipment investment required, mild operating conditions, and efficient utilization of energy [1–4]. During adsorption processes, it is essential to be able to selectively remove the target substances from mixtures and to efficiently release the adsorbates for regeneration, since doing so is strongly associated with product quality and with the input time and energy [5]. As adsorbents play a critical role in adsorption processes, achieving efficient adsorption and desorption processes by controllably tuning the properties of adsorbents at different technical stages is extremely attractive [6–9]. However, it is difficult for traditional adsorbents to reach the target due to their fixed active sites. To be specific, the active sites of traditional adsorbents can be easily accessed by all adsorbates when the pore sizes are sufficiently large. This results in low selectivity, such that the product purity cannot meet the increasing industrial requirements. Modulating the pore sizes or constructing target-specific

sites in traditional adsorbents can promote selectivity, but results in a problem: The release of adsorbates becomes difficult. This problem is caused by increased diffusion resistance or enhanced adsorbate–adsorbent interactions, and inevitably gives rise to difficulty in desorption and intensive energy consumption. The tradeoff between selective adsorption and efficient desorption poses enormous challenges when devising and synthesizing desirable adsorbents [10]. As adsorption and desorption are sequential stages in adsorption processes, the technical efficiency can be remarkably improved if adsorbents can be made to be responsive to external stimuli and to shelter or expose their active sites on demand. This concept is very different from the traditional concept, in which variation of the adsorption capacity depends on the cyclic variation of pressure and/or temperature, which requires massive energy consumption.

Inspired by living systems that can adjust themselves to changeable environments for survival, functional materials that are responsive to external stimuli with structurally or chemically switchable properties have been engineered to perform various roles for practical application in recent years [11–15]. The external stimuli include light [16–19], temperature [20–23], pH [24–28], and redox reactions [29–32]. Among these diverse forms of stimulation, light has been given particular attention because it permits

* Corresponding authors.
   E-mail addresses: liuxq@njtech.edu.cn (X.-Q. Liu), lbsun@njtech.edu.cn (L.-B. Sun).

fast and precise control and generates few undesired byproducts. As typical photoresponsive molecules, azobenzenes can reversibly transform between *cis* and *trans* isomerization through stimulation with ultraviolet (UV) light and visible (Vis) light [33–35]. This isomerization causes azobenzene and its derivatives to change conformation between the rod-like and curved states. Based on this conformational change, azobenzenes are promising candidates for sheltering and exposing active sites to adsorbates in a manner that is well tuned by UV/Vis irradiation on demand [36–39]. It is worth noting that this target requires suitable pore sizes in the supports. Macroporous/mesoporous materials have relatively large pore sizes; thus, both large and small molecules can pass through the pore channels and come into contact with active sites, resulting in the failure of selective adsorption [40–42]. Although microporous materials with relatively small pore sizes can hinder the entrance of large molecules, it is difficult for the adsorbed substances to be released after adsorption [43,44]. Consequently, mesoporous materials with pore sizes of around 2–5 nm are good candidates for capturing both small and large molecules. The rational introduction of photoresponsive molecules can endow mesoporous materials with tunable selectivity and decrease the energy consumption required for desorption.

In this work, molecular switches—namely, 4-(3-triethoxysilyl propyl-ureido)azobenzene (AB-TPI)—were introduced into mesopores during the synthesis of Ce-doped mobile composition of matters (MCM)-41 (denoted herein as CeM). Cerium (Ce) was doped in order to generate additional active sites to enhance the adsorption performance [45–48]. The relatively large molecule methylene blue (MB) and the relatively small molecule brilliant blue (BB) were employed to test the adsorption performance. The results show that Ce doping leads to a remarkable increase of 13.5% and 65.5%, respectively, in the capacity of MCM-41 to separately capture MB and BB. AB-TPI molecules act as molecular switches that alternately shelter and expose active sites through photoisomerization. To be specific, the *cis* isomers with curved states are close to the active sites in space, and thus have steric effects on relatively large molecules while negligibly affecting the approach of relatively small molecules (Fig. 1(a)). When AB-TPI transforms into the *trans* configuration, it fully exposes the active sites, allowing the attached adsorbates to be easily released, and

achieving efficient desorption (Fig. 1(b)). As a result, these molecular switches can reversibly regulate adsorption and desorption. Triggered by UV/Vis light, such smart adsorbents display excellent performance in selective adsorption and efficient desorption, and thus provide clues for the development of controllable adsorbents for energy efficiency.

2. Experimental section

2.1. Chemicals

3-(Triethoxysilyl)propyl isocyanate (TESPIC), cetyltrimethylammonium bromide (CTAB), tetraethylorthosilicate (TEOS), and $Ce(SO_4)_2 \cdot 4H_2O$ were purchased from Sigma-Aldrich Co., USA. 4-Phenylazoaniline (PAA) was produced by Tokyo Chemical Industry (TCI) Co., Ltd., Japan. Methanol, hexane, toluene, and tetrahydrofuran (THF) were purchased from Aladdin, China. The trace amount of water in the toluene and THF was removed by a 4A molecular sieve before using; the other chemicals were used without further purification.

2.2. Materials synthesis

The photoresponsive molecule AB-TPI was prepared using a procedure similar to that reported in the literature (Supplementary data Fig. S1) [49]. 1.58 g of PAA and 2.05 g of TESPIC were first mixed in 12 mL of anhydrous THF. The mixture was then transferred to a Pyrex tube under a nitrogen (N_2) atmosphere. After heating at 65 °C for 12 h, 40 mL of hexane was added to the mixture. The parent materials were then incubated overnight at 20 °C. Orange crystals were obtained after washing the solid products three times with hexane.

MCM-41 was prepared based on a previous method [50]. 3.5 mL of NaOH and 1.00 g of CTAB were mixed in 480 mL of water, and the solution was heated to 80 °C. Next, TEOS (5 mL) was added dropwise to the solution with vigorous stirring. After reacting for 2 h, the white silica colloidal suspension was filtered, and the obtained solids were washed with water several times. The obtained solids were then dispersed in ethanol (100 mL) and HCl (1 mol·L^{-1}, 1 mL), followed by refluxing at 80 °C for 6 h. Finally,
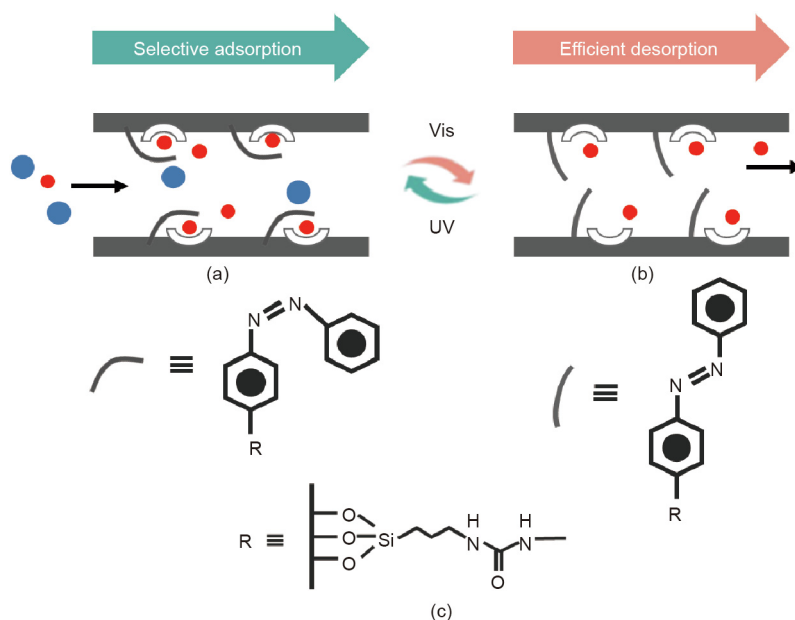
Fig. 1. (a) Illustration of the selective adsorption of smart adsorbents with AB-TPI in the *cis* configuration; (b) efficient desorption with AB-TPI in the *trans* configuration; (c) *cis*/*trans* isomerization of AB-TPI by UV/Vis light irradiation.

the extracted template was removed by washing the products with ethanol several times. The process of preparing CeM was similar to the process used to prepare MCM-41, but 0.18 g of $Ce(SO_4)_2 \cdot 4H_2O$ was initially added to the mixture.

The smart azobenzene-functionalized adsorbents were prepared by *in situ* synthesis. 3.5 mL of NaOH with a concentration of 2 mol·L^{-1} and 1.00 g of CTAB were mixed in 480 mL of water. Next, TEOS (5 mL) and a certain amount of AB-TPI (see below) was added dropwise to the solution with vigorous stirring. The subsequent steps were the same as those used with MCM-41. The obtained samples were denoted as Azo-CeM-1, Azo-CeM-2, Azo-CeM-3, and Azo-CeM-4, corresponding to the added AP-TPI amounts of 34.7, 69.4, 138.7, and 218.0 mg, respectively.

2.3. Materials characterization

^{1}H and ^{13}C nuclear magnetic resonance (NMR) was performed on a Bruker AVANCE NEO spectrometer (400 MHz, Bruker Corporation, USA) in dimethyl sulfoxide. X-ray diffraction (XRD) patterns were collected by a Rigaku D/MAX-γA with CuKα radiation (Rigaku Corporation, Japan). Scanning electron microscopy (SEM) was performed on a Hitachi New Generation SU8010 electron microscope (Hitachi, Ltd., Japan). The metal content of different samples was determined using energy-dispersive X-ray (EDX) analyses with Kevex equipment attached to the scanning microscope. Transmission electron microscope (TEM) images were collected using an FEI Tecnai G2 F20 electron microscope (FEI Company, Japan) operated at an acceleration voltage of 200 kV. N$_2$ adsorption–desorption tests were performed on an ASAP 2020 analyzer (GAT Scientific Sdn Bhd, Malaysia) at −196 °C, and samples were pretreated at 100 °C in a high vacuum for 4 h. The Brunauer–Emmett–Teller (BET) surface area was obtained according to the adsorption data, with relative pressure (p/p_0) ranging from 0.04 to 0.20. The Barrett–Joyner–Halenda (BJH) method was employed to calculate the pore size distributions, based on the adsorption branches of the isotherms. UV–Vis spectra were recorded on a PerkinElmer Lambda 35 spectrometer (PerkinElmer Inc., USA) with wavelengths from 300 to 600 nm. Fourier-transform infrared (IR) spectra were obtained with wavelengths from 550 to 4000 nm (Nicolet Nexus 470, Thermo Fisher Scientific Inc., USA). The content of the elements carbon (C), hydrogen (H), and nitrogen (N) was obtained by an elemental analyzer from Elementar Analysensysteme GmbH, Germany. Thermogravimetric (TG) analysis was carried out on an STA-499C (NETZSCH, Germany) with a heating rate of 20 °C·min^{-1}.

2.4. Adsorption experiments

For the selective adsorption study, the azobenzene groups of the adsorbents remained as *cis* isomers; thus, the active sites were sheltered from the relatively large molecules. Two dye molecules, MB and BB, were chosen as the adsorbates. In a typical experiment, one of the adsorbates (3 mL, 25 mg·L^{-1}) was added in a cuvette containing 2 mg of adsorbent. The system was treated with UV light (365 nm) for 3 h. The amount adsorbed (Q_e) was determined according to Eq. (1).

$$Q_e = \frac{(c_i - c_e)V}{m} \tag{1}$$

where c_i is the initial concentration, c_e is the equilibrium concentration, V is the volume of water, and m is the mass of adsorbent.

For the desorption study, the azobenzene groups of the adsorbent were transformed from *cis* to *trans* isomers; thus, the active sites were exposed. In a typical experiment, the saturated adsorbent was irradiated with Vis light with a wavelength of 450 nm for 180 min. An ethanol/water mixture was used to wash the adsorbent. The concentration of the desorbed adsorbate was determined at regular intervals. The amount desorbed (Q_d) was calculated based on Eq. (2):

$$Q_d = \frac{c_d V}{mQ_e} \times 100\% \tag{2}$$

where c_d refers to the equilibrium concentration during desorption.

3. Results and discussion

3.1. Textural and structural properties

AB-TPI was first analyzed by ^{1}H and ^{13}C NMR (Figs. S2(a) and (b)). The characteristic resonances clearly showed the successful synthesis of AB-TPI [19]. No other undefined resonances were observed, suggesting few impurities in the products. After removing the template, the photoresponsive groups were modulated to shelter and expose the active sites. The grafted amounts of the photoresponsive groups on Azo-CeM-1, Azo-CeM-2, Azo-CeM-3, and Azo-CeM-4 were calculated as 5.6 wt%, 7.8 wt%, 12.6 wt%, and 17.8 wt%, respectively (Table 1).

The structural information of the materials was analyzed by means of XRD patterns. Fig. 2(a) shows the low-angle XRD pattern of CeM. The prominent peak at the 2θ angle of 2.4 can be assigned to the reflection of (100) interplanar spacing (d_{100}). This represents the two-dimensional (2D) hexagonal pore symmetry of MCM-41 (Fig. S3(a)) [51,52]. The diffraction peaks of Azo-CeM-1, Azo-CeM-2, Azo-CeM-3, and Azo-CeM-4 are the same as those of CeM, indicating that the azobenzene groups have little effect on the structure of CeM. The wide-angle XRD patterns of the different samples were also recorded. MCM-41 displays only one broad diffraction peak centered around 23° (Fig. S3(b)) [53–55]. After Ce is introduced, three diffraction peaks at the 2θ angle of 28°, 47°, and 56° can be observed (Fig. 2(b)). These peaks can be ascribed to the d_{111}, d_{220}, and d_{311} reflections of a typical CeO$_2$ phase (Joint Committee on Powder Diffraction Standards (JCPDS) no. 034-0394) [56]. It should be stated that these new peaks are weak and broad, implying that the CeO$_2$ is well dispersed.

Table 1
Physicochemical parameters and elemental composition of different samples.

Sample	Grafted amount of AB-TPI[a] (wt%)	S_{BET}[b] (m^2·g^{-1})	V_p[c] (cm^3·g^{-1})	Elemental composition (wt%)		
				N	C	H
CeM	0.0	971	0.93	—	—	—
Azo-CeM-1	5.6	933	1.07	0.70	5.87	1.12
Azo-CeM-2	7.8	902	0.94	0.98	7.80	1.05
Azo-CeM-3	12.6	873	0.91	1.59	9.50	1.04
Azo-CeM-4	17.8	825	0.79	2.24	11.78	1.50

[a] The introduced amount was calculated based on elemental analysis.
[b] The BET surface area (S_{BET}) was calculated using adsorption data in relative pressures ranging from 0.04 to 0.20.
[c] The pore volume (V_p) was determined from the amount adsorbed at a relative pressure of 0.99.
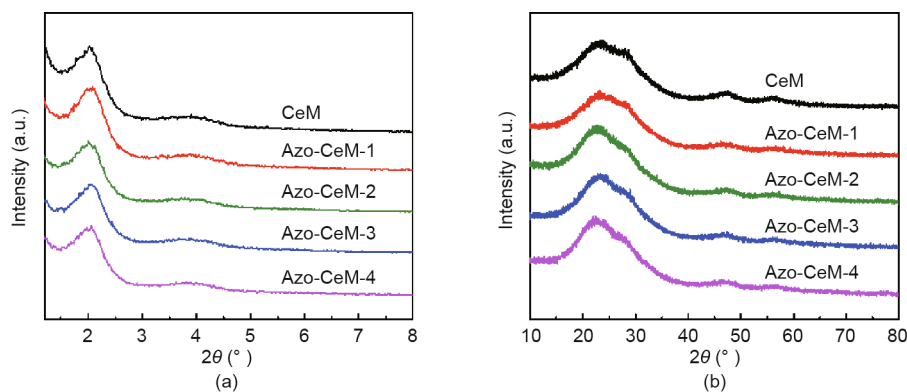
Fig. 2. (a) Low-angle and (b) wide-angle XRD patterns of different samples.

N_2 adsorption–desorption tests were conducted to study the pore structures. Figs. 3(a) and S4(a) show that all the samples displayed typical type-IV isotherms. A remarkable increase can be observed at relative pressure from 0.3 to 0.4, indicating the abundant mesopores of different samples. MCM-41 has a BET surface area of 1224 $m^2 \cdot g^{-1}$, suggesting that it has highly developed open pores (Table S1). After the introduction of Ce, this value decreases to 971 $m^2 \cdot g^{-1}$ (Table 1). The introduction of photoresponsive groups further decreases the surface area, although it is still maintained at a high level. For example, the surface area of Azo-CeM-4, which has the greatest amount of grafting, is as high as 825 $m^2 \cdot g^{-1}$. Figs. 3(b) and S4(b) show that the pore size distributions of different samples are narrow. The apertures of most mesopores are around 2.9 nm, which is suitable for the stretching and bending of the azobenzene groups. In addition, the mesoporous structure can be well maintained after Ce doping and the AB-TPI grafting reaction. However, compared with MCM-41, CeM exhibits a decrease of pore volume, and the introduction of AB-TPI also results in a declining trend in pore volume with increasing amounts of AB-TPI. This finding confirms that the active sites and AB-TPI were introduced into the pore channels of MCM-41. Azo-CeM-3 presented identical N_2 adsorption behavior in the *trans* and *cis* configurations (Fig. S5). This is because the size of an N_2 molecule is relatively small.

TEM and SEM images were employed to observe the morphology of the adsorbents. As shown in the SEM images (Fig. S6), the MCM-41 particles were regular spheres. CeM had a suborbicular morphology with relatively large particles, and some pieces were packed on the surface. This is probably due to the slight aggregation of particles caused by Ce doping. No further aggregation was observed for Azo-CeM-3, indicating that the AB-TPI grafting had little impact on the morphology. The TEM images clearly show the pore channels of Azo-CeM-3 (Fig. 4(a)). The uniform and straight pore channels of Azo-CeM-3 are important for the capture of adsorbates. This observation supports the XRD and N_2 adsorption results, which indicate that the pore structures were well preserved during synthesis, despite some aggregation of adsorbent particles.

The identification of AB-TPI and the thermal stability of the adsorbents were demonstrated by the following techniques. As shown by the EDX analysis (Fig. S7), Azo-CeM-3 was composed of the elements C, N, oxygen (O), silicon (Si), and Ce; the EDX mapping (Fig. 4(b)) clearly shows that these elements were uniformly dispersed in the frameworks. The main organic groups and covalent bonds of the adsorbents were measured by means of IR spectra (Figs. 5(a) and S8(a)). For MCM-41, the band at 957 cm^{-1} can be ascribed to the stretching vibrations of the silanol groups. The bands at 1086 and 797 cm^{-1} can be respectively assigned to the asymmetric and symmetric stretching vibrations of the Si–O–Si frameworks [57,58]. For the other samples, the characteristic bands of MCM-41 can be clearly observed. After introducing AB-TPI, three new bands appear. The band at 1548 cm^{-1} can be ascribed to the stretching vibration of –NH–CO–NH–, the band at 1502 cm^{-1} corresponds to the stretching vibration of –NH–, and the band at 688 cm^{-1} can be assigned to the vibration of the aromatic amine [49]. These results confirm the successful introduction of AB-TPI; furthermore, the intensity of these characteristic bands increases as more AB-TPI groups are introduced. The weak vibrational band at around 2950 cm^{-1} is attributed to the vibration of the carbon chains of CTAB, and derives from its incomplete removal by extraction. TG analysis was performed to test the thermal stability of different samples (Figs. 5(b) and S8(b)). The results
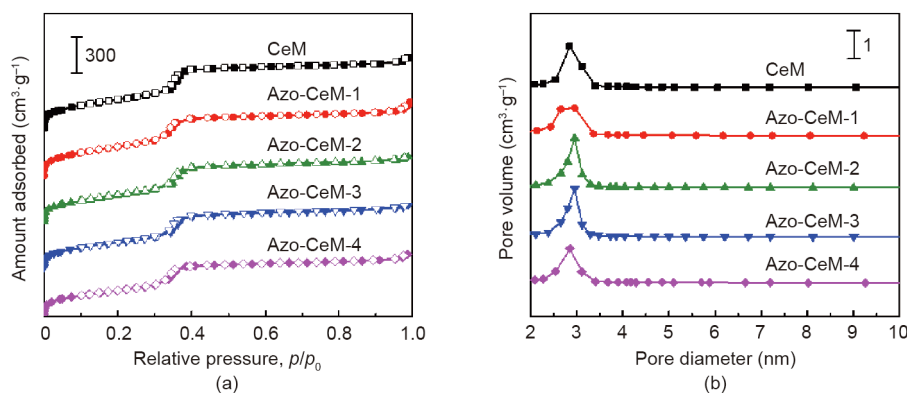

Fig. 3. (a) N_2 adsorption–desorption isotherms and (b) pore size distributions of different samples. The curves are offset on the *y* axis for clarity.
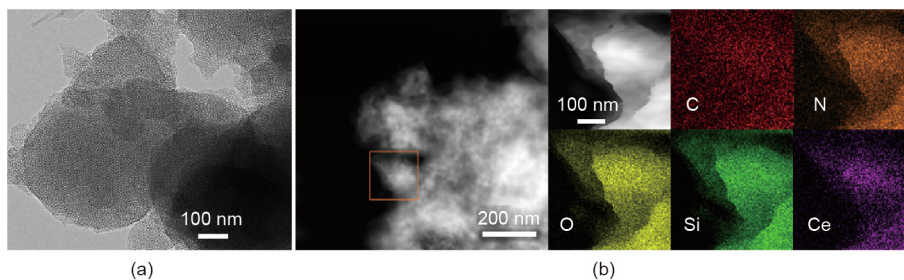
Fig. 4. (a) TEM image of Azo-CeM-3 and (b) its EDX mapping images of the C, N, O, Si, and Ce elements.
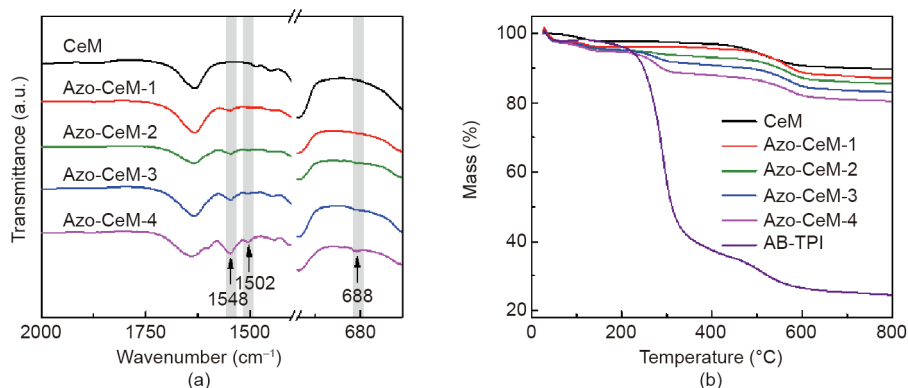

Fig. 5. (a) IR spectra and (b) TG curves of different samples.

show that AB-TPI decomposed in the temperature interval from 200 to 700 °C, and the residual template CTAB decomposed in the temperature interval from 500 to 600 °C.

3.2. Photoresponsive properties

The photoisomerization of AB-TPI (dissolved in ethanol) was recorded by means of UV/Vis spectroscopy. As shown in Fig. 6, two bands around 350 and 450 nm were observed, which correspond to the π-to-π* and n-to-π* transitions of the π-conjugated system for AB-TPI. UV irradiation resulted in an intensity decline of the broad band at 360 nm, while leading to an intensity increase of the broad band at 450 nm. This result corresponds to the isomerization of AB-TPI from the *trans* to *cis* isomer. When the irradiation
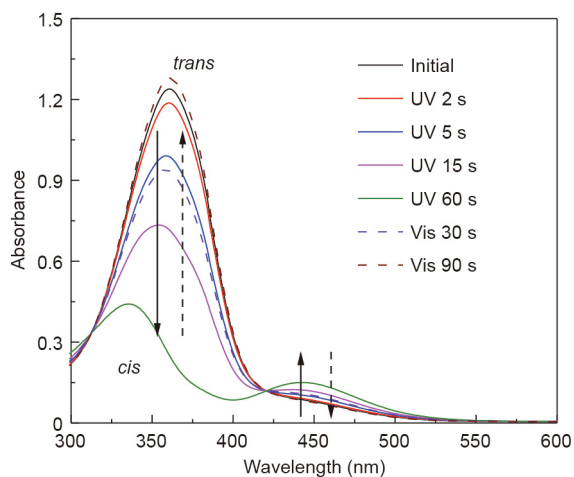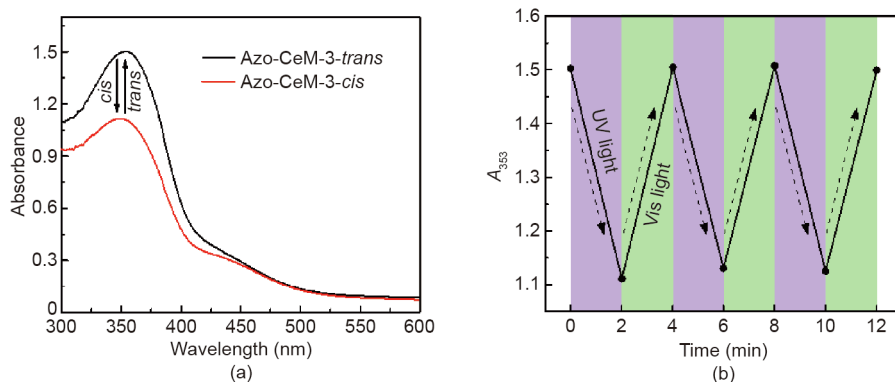

Fig. 6. Alteration in the UV–Vis spectra of AB-TPI upon UV/Vis light irradiation.

time reached 60 s, AB-TPI reaches a photostationary state. UV irradiation recovered the adsorption intensity of the two bands, which corresponds to the conformational change of AB-TPI from the *cis* to the *trans* configuration. The intensity of the 350 nm band became stronger than that of the pure AB-TPI when the irradiation time was longer than 90 s. This result indicates that some azobenzene groups initially exist as *cis* isomers. Through cyclic variations of UV and Vis, the AB-TPI is able to switch between the *trans* and *cis* configurations (Figs. S9(a) and (b)), reversibly acting as molecule switches modulated by photostimulation. After Ce and AB-TPI are introduced into the pore channels of MCM-41, photoisomerization of the azobenzene groups can be achieved. Taking Azo-CeM-3 as an example, its UV–Vis spectrum (Figs. 7(a) and (b)) exhibited the same change as pure AB-TPI upon UV or Vis irradiation. In addition, the photoisomerization was reversible after three cycles. Thus, it is confirmed that the photoresponsiveness of the azobenzene groups was well maintained after immobilization on MCM-41. On this basis, switching of the active sites by means of AB-TPI is likely, and may have significant effects on adsorption and desorption.

3.3. Adsorption performance

Two probing molecules were employed to demonstrate the promoting effects of doping with Ce and the influence of the photoresponsive groups on adsorption. MB was used as a relatively small molecule, with a size of 1.26 nm, while BB was used as a relatively large molecule, with a size of 1.98 nm (Fig. S10). The effects of Ce doping on adsorption were investigated first. Compared with MCM-41 (Fig. S11(a)), CeM exhibited an obviously larger adsorption capacity for both MB and BB (Figs. S12(a) and S13(a)), indicating that Ce doping resulted in an increased number of active sites. As MB is a weak Lewis base [59], it can be captured through acid-base interactions between the dye molecules and the active sites on the adsorbents' surfaces. Ce doping increases the electron-pair

Fig. 7. (a) Alteration in the UV–Vis spectra of Azo-CeM-3 upon UV/Vis light irradiation; (b) reversible changes in absorbance at 353 nm (A_{353}) as a function of cycles for Azo-CeM-3.

donation to the inner-side pore wall surface, forming Lewis acid centers that promote the Lewis acidity of the adsorbents [60]. For the capture of BB, which is an anionic dye, Ce doping can promote cationic–anionic interactions between BB molecules and the modified surfaces. The positively charged surface of the adsorbents contributes to the electrostatic attraction between the adsorbates and adsorbents [61–63]. Consequently, Ce doping provided additional active sites for capturing both MB and BB.

Next, the influence of the photoresponsive groups was investigated. Upon UV light irradiation, CeM displayed an inconspicuous change in the amount adsorbed of both MB and BB, which indicates that external photostimulation cannot interfere with the adsorption performance of CeM. After sheltering the active sites, the capacities of the photoresponsive samples exhibited insignificant differences for MB (Figs. S12(b), (c), and (d)), but showed remarkable declines for BB (Figs. S13(b), (c), and (d)). Taking Azo-CeM-3 as an example, its capacity for MB slightly decreased from 22.4 to 20.5 mg·g^{-1} (Fig. 8(a)). Interestingly, an obvious decrease in capacity of around 43% (from 13.8 to 7.8 mg·g^{-1}, Fig. 8(b)) was observed for BB after UV light irradiation. This result suggests that Azo-CeM-3 has excellent selectivity for MB over BB after photostimulation. We propose that steric hindrance derived from the photoisomerization of AB-TPI in MCM-41 explains this phenomenon. After UV light irradiation, the active sites in the pore channels of the adsorbents are switched off by the AB-TPI in the *cis* configuration. In this case, the active sites are sheltered by the curved structure of the photoresponsive groups, making it difficult for the relatively large BB molecules to access them. In contrast, the relatively small MB

molecules can pass freely through the confined spaces and be adsorbed by the active sites.

The loading amount of AB-TPI was further modulated, and the corresponding effects on adsorption were investigated. As shown in Fig. 9, although more AB-TPI groups were introduced to CeM, a change in isotherms for MB was not obvious before and after UV light irradiation. This result confirms that MB molecules cannot be excluded by photoresponsive groups. It was notable that BB capture became difficult after UV light irradiation, and the adsorption capacity decreased as the loading amount of AB-TPI increased. It should be stated that when excessive AB-TPI groups are loaded, the adsorption capacity is adversely affected because the ordering of MCM-41 decreases and the pore channels can be blocked. The optimal sample was Azo-CeM-3, with a variation of 43% in capacity. This finding indicates that the variation in the spatial configuration of AB-TPI greatly interferes—through steric hindrance—with the approach of BB molecules to the active sites, thus providing an efficient and energy-saving method to vary the adsorption capacity.

The desorption performance was explored on Azo-CeM-3 saturated by MB. As shown in Fig. 10, the obtained desorption amount reached as high as 97.4% with AB-TPI in the *trans* configuration. However, only 68.3% of the adsorbates were released with AB-TPI in the *cis* configuration. This finding indicates that the exposure of active sites contributes to desorption when AB-TPI is transformed to the *trans* configuration. Finally, the reusability of Azo-CeM-3 was studied. As shown in Fig. 11, there was insignificant loss in capacity after five cycles, suggesting excellent recyclability.
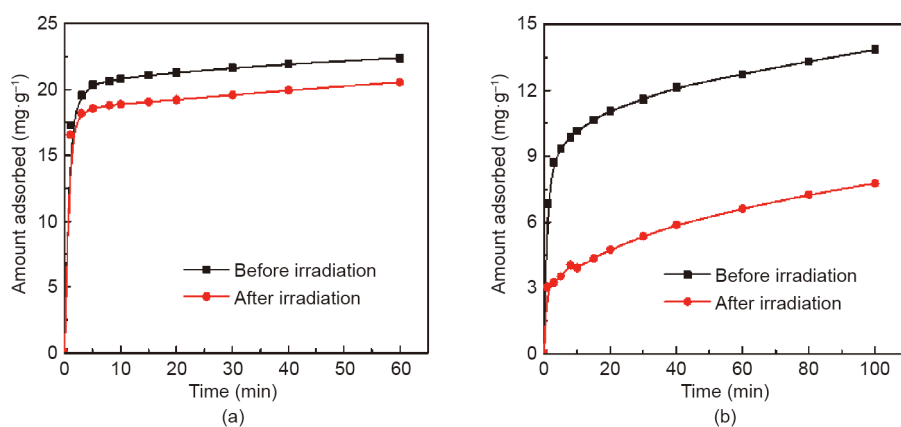
Fig. 8. Dynamic adsorption curves of (a) MB and (b) BB on Azo-CeM-3 before and after UV light irradiation.
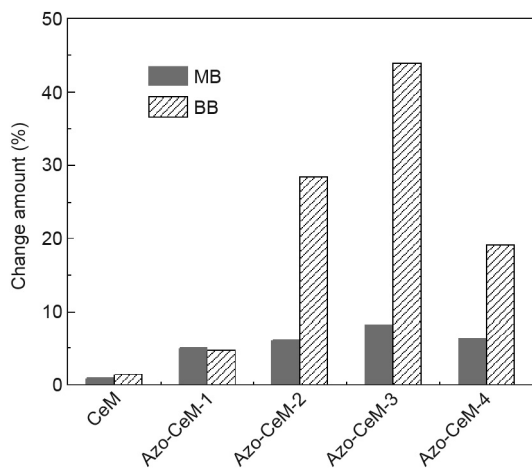
Fig. 9. Change in the adsorption capacity on MB and BB over different adsorbents before and after UV light irradiation.
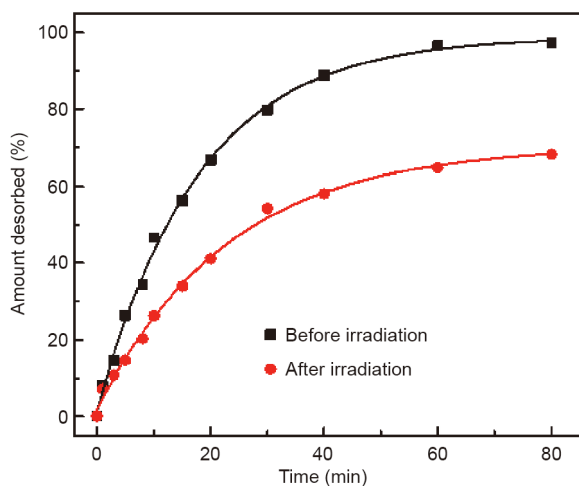

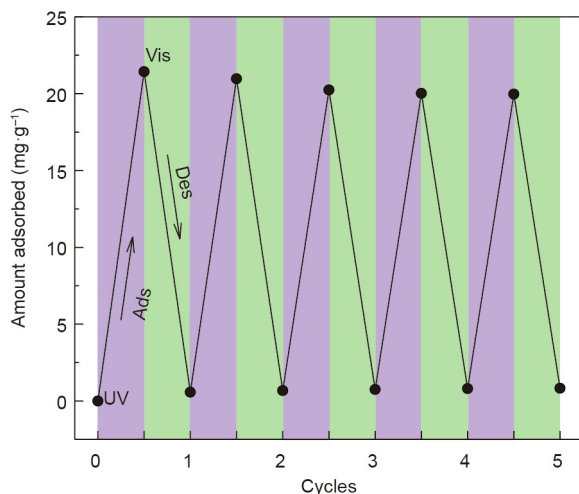**Fig. 10.** Desorption curves of MB on Azo-CeM-3 before and after UV light irradiation.

Fig. 11. Adsorption/desorption cycles of MB on Azo-CeM-3 under UV/Vis light irradiation. Ads: adsorption; Des: desorption.

4. Conclusions

In summary, Ce-doped smart adsorbents with photoresponsive molecular switches were successfully fabricated. Ce was doped to provide additional active sites for enhancing adsorption performance. Through the precise sheltering and exposing of active sites by photoresponsive groups, the smart adsorbents exhibited excellent performance in selective adsorption and efficient desorption. Moreover, the adsorption and desorption processes could be regulated reversibly by these molecular switches. These smart adsorbents displayed a remarkable performance in selective adsorption and efficient desorption, giving clues for the development of controllable adsorbents for energy efficiency. Furthermore, this new conception with the introduction of stimuli-responsive molecules should be transferrable to other adsorbents, thus extending the application of light energy in adsorption to protect the environment and increase energy efficiency.

Acknowledgements

Compliance with ethics guidelines

Peng Tan, Yao Jiang, Shi-Chao Qi, Xia-Jun Gao, Xiao-Qin Liu, and Lin-Bing Sun declare that they have no conflict of interest or financial conflicts to disclose.

Appendix A. Supplementary data

Supplementary data to this article can be found online at https://doi.org/10.1016/j.eng.2020.03.005.

References

[1] Li L, Lin RB, Krishna R, Li H, Xiang S, Wu H, et al. Ethane/ethylene separation in a metal–organic framework with iron–peroxo sites. Science 2018;362(6413):443–6.
[2] Reed DA, Keitz BK, Oktawiec J, Mason JA, Runčevski T, Xiao DJ, et al. A spin transition mechanism for cooperative adsorption in metal–organic frameworks. Nature 2017;550(7674):96–100.
[3] Cui X, Chen K, Xing H, Yang Q, Krishna R, Bao Z, et al. Pore chemistry and size control in hybrid porous materials for acetylene capture from ethylene. Science 2016;353(6295):141–4.
[4] Tan P, Xue DM, Zhu J, Jiang Y, He QX, Hou Z, et al. Hierarchical N-doped carbons from designed N-rich polymer: adsorbents with a record-high capacity for desulfurization. AIChE J 2018;64(11):3786–93.
[5] Li JR, Yu J, Lu W, Sun LB, Sculley J, Balbuena PB, et al. Porous materials with pre-designed single-molecule traps for CO2 selective adsorption. Nat Commun 2013;4:1538.
[6] Flytzani-Stephanopoulos M, Sakbodin M, Wang Z. Regenerative adsorption and removal of H2S from hot fuel gas streams by rare earth oxides. Science 2006;312(5779):1508–10.
[7] Sun LB, Li JR, Lu W, Gu ZY, Luo Z, Zhou HC. Confinement of metal–organic polyhedra in silica nanopores. J Am Chem Soc 2012;134(38):15923–8.
[8] Kang YH, Liu XD, Yan N, Jiang Y, Liu XQ, Sun LB, et al. Fabrication of isolated metal–organic polyhedra in confined cavities: adsorbents/catalysts with unusual dispersity and activity. J Am Chem Soc 2016;138(19):6099–102.
[9] Jiang WJ, Yin Y, Liu XQ, Yin XQ, Shi YQ, Sun LB. Fabrication of supported cuprous sites at low temperatures: an efficient, controllable strategy using vapor-induced reduction. J Am Chem Soc 2013;135(22):8137–40.
[10] Jiang Y, Shan SF, Liu W, Zhu J, He QX, Tan P, et al. Rational design of thermo-responsive adsorbents: demand-oriented active sites for the adsorption of dyes. Chem Commun 2017;53(69):9538–41.
[11] Theato P, Sumerlin BS, O'Reilly RK, Epps TH 3rd. Stimuli responsive materials. Chem Soc Rev 2013;42(17):7055–6.
[12] Nath N, Chilkoti A. Creating, "smart" surfaces using stimuli responsive polymers. Adv Mater 2002;14(17):1243–7.

[13] Mendes PM. Stimuli-responsive surfaces for bio-applications. Chem Soc Rev 2008;37(11):2512–29.

[14] Roy D, Cambre JN, Sumerlin BS. Future perspectives and recent advances in stimuli-responsive materials. Prog Polym Sci 2010;35(1–2):278–301.

[15] Stuart MA, Huck WT, Genzer J, Müller M, Ober C, Stamm M, et al. Emerging applications of stimuli-responsive polymer materials. Nat Mater 2010;9 (2):101–13.

[16] Li P, Xie G, Kong XY, Zhang Z, Xiao K, Wen L, et al. Light-controlled ion transport through biomimetic DNA-based channels. Angew Chem Int Ed Engl 2016;55(50):15637–41.

[17] Liu N, Dunphy DR, Rodriguez MA, Singer S, Brinker J. Synthesis and crystallographic structure of a novel photoresponsive azobenzene-containing organosilane. Chem Commun 2003;10:1144–5.

[18] Yagai S, Kitamura A. Recent advances in photoresponsive supramolecular self-assemblies. Chem Soc Rev 2008;37(8):1520–9.

[19] Zhu J, Tan P, Yang PP, Liu XQ, Jiang Y, Sun LB. Smart adsorbents with reversible photo-regulated molecular switches for selective adsorption and efficient regeneration. Chem Commun 2016;52(77):11531–4.

[20] Moon HJ, Ko DY, Park MH, Joo MK, Jeong B. Temperature-responsive compounds as *in situ* gelling biomedical materials. Chem Soc Rev 2012;41 (14):4860–83.

[21] Yu Z, Li N, Zheng P, Pan W, Tang B. Temperature-responsive DNA-gated nanocarriers for intracellular controlled release. Chem Commun 2014;50 (26):3494–7.

[22] Yue M, Hoshino Y, Ohshiro Y, Imamura K, Miura Y. Temperature-responsive microgel films as reversible carbon dioxide absorbents in wet environment. Angew Chem Int Ed Engl 2014;53(10):2654–7.

[23] Ding JJ, Zhu J, Li YX, Liu XQ, Sun LB. Smart adsorbents functionalized with thermoresponsive polymers for selective adsorption and energy-saving regeneration. Ind Eng Chem Res 2017;56(15):4341–9.

[24] Park C, Oh K, Lee SC, Kim C. Controlled release of guest molecules from mesoporous silica particles based on a pH-responsive polypseudorotaxane motif. Angew Chem Int Ed Engl 2007;46(9):1455–7.

[25] Yu X, Wang Z, Jiang Y, Shi F, Zhang X. Reversible pH-responsive surface: from superhydrophobicity to superhydrophilicity. Adv Mater 2005;17(10): 1289–93.

[26] Lee CH, Cheng SH, Huang IP, Souris JS, Yang CS, Mou CY, et al. Intracellular pH-responsive mesoporous silica nanoparticles for the controlled release of anticancer chemotherapeutics. Angew Chem Int Ed Engl 2010;49(44):8214–9.

[27] Krämer M, Stumbé JF, Türk H, Krause S, Komp A, Delineau L, et al. pH-responsive molecular nanocarriers based on dendritic core-shell architectures. Angew Chem Int Ed Engl 2002;41(22):4252–6.

[28] Das M, Mardyani S, Chan WCW, Kumacheva E. Biofunctionalized pH-responsive microgels for cancer cell targeting: rational design. Adv Mater 2006;18(1):80–3.

[29] Li ZY, Hu JJ, Xu Q, Chen S, Jia HZ, Sun YX, et al. A redox-responsive drug delivery system based on RGD containing peptide-capped mesoporous silica nanoparticles. J Mater Chem B 2015;3(1):39–44.

[30] Nguyen TD, Liu Y, Saha S, Leung KC, Stoddart JF, Zink JI. Design and optimization of molecular nanovalves based on redox-switchable bistable rotaxanes. J Am Chem Soc 2007;129(3):626–34.

[31] Wang C, Guo Y, Wang Y, Xu H, Zhang X. Redox responsive supramolecular amphiphiles based on reversible charge transfer interactions. Chem Commun 2009;36:5380–2.

[32] Li XQ, Wen HY, Dong HQ, Xue WM, Pauletti GM, Cai XJ, et al. Self-assembling nanomicelles of a novel camptothecin prodrug engineered with a redox-responsive release mechanism. Chem Commun 2011;47(30):8647–9.

[33] Bandara HM, Burdette SC. Photoisomerization in different classes of azobenzene. Chem Soc Rev 2012;41(5):1809–25.

[34] Liu N, Yu K, Smarsly B, Dunphy DR, Jiang YB, Brinker CJ. Self-directed assembly of photoactive hybrid silicates derived from an azobenzene-bridged silsesquioxane. J Am Chem Soc 2002;124(49):14540–1.

[35] Manna D, Udayabhaskararao T, Zhao H, Klajn R. Orthogonal light-induced self-assembly of nanoparticles using differently substituted azobenzenes. Angew Chem Int Ed Engl 2015;54(42):12394–7.

[36] Park J, Yuan D, Pham KT, Li JR, Yakovenko A, Zhou HC. Reversible alteration of CO₂ adsorption upon photochemical or thermal treatment in a metal–organic framework. J Am Chem Soc 2012;134(1):99–102.

[37] Alvaro M, Benitez M, Das D, Garcia H, Peris E. Reversible porosity changes in photoresponsive azobenzene-containing periodic mesoporous silicas. Chem Mater 2005;17(20):4958–64.

[38] Liu N, Chen Z, Dunphy DR, Jiang YB, Assink RA, Brinker CJ. Photoresponsive nanocomposite formed by self-assembly of an azobenzene-modified silane. Angew Chem Int Ed Engl 2003;42(15):1731–4.

[39] Brown JW, Henderson BL, Kiesz MD, Whalley AC, Morris W, Grunder S, et al. Photophysical pore control in an azobenzene-containing metal–organic framework. Chem Sci 2013;4(7):2858–64.

[40] Awala H, Gilson JP, Retoux R, Boullay P, Goupil JM, Valtchev V, et al. Template-free nanosized faujasite-type zeolites. Nat Mater 2015;14(4):447–51.

[41] Gibson LT. Mesosilica materials and organic pollutant adsorption: part B removal from aqueous solution. Chem Soc Rev 2014;43(15):5173–82.

[42] Li W, Zhao D. An overview of the synthesis of ordered mesoporous materials. Chem Commun 2013;49(10):943–6.

[43] Brochard L, Vandamme M, Pellenq RJ, Fen-Chong T. Adsorption-induced deformation of microporous materials: coal swelling induced by CO₂–CH₄ competitive adsorption. Langmuir 2012;28(5):2659–70.

[44] Kondo M, Shimamura M, Noro S, Minakoshi S, Asami A, Seki K, et al. Microporous materials constructed from the interpenetrated coordination networks. Structures and methane adsorption properties. Chem Mater 2000;12(5):1288–99.

[45] Laha SC, Mukherjee P, Sainkar SR, Kumar R. Cerium containing MCM-41-type mesoporous materials and their acidic and redox catalytic properties. J Catal 2002;207(2):213–23.

[46] He X, Antonelli D. Recent advances in synthesis and applications of transition metal containing mesoporous molecular sieves. Angew Chem Int Ed Engl 2002;41(2):215–29.

[47] Calles JA, Carrero A, Vizcaíno AJ. Ce and La modification of mesoporous Cu-Ni/ SBA-15 catalysts for hydrogen production through ethanol steam reforming. Microporous Mesoporous Mater 2009;119(1–3):200–7.

[48] Pal N, Mukherjee I, Chatterjee S, Cho EB. Surfactant-assisted synthesis of ceria-titania-rich mesoporous silica materials and their catalytic activity towards photodegradation of organic dyes. Dalton Trans 2017;46(29):9577–90.

[49] Cheng L, Jiang Y, Yan N, Shan SF, Liu XQ, Sun LB. Smart adsorbents with photoregulated molecular gates for both selective adsorption and efficient regeneration. ACS Appl Mater Interfaces 2016;8(35):23404–11.

[50] Cheng L, Jiang Y, Qi SC, Liu W, Shan SF, Tan P, et al. Controllable adsorption of CO₂ on smart adsorbents: an interplay between amines and photoresponsive molecules. Chem Mater 2018;30(10):3429–37.

[51] Jiang Y, Tan P, Kang YH, Xing ZM, Cheng L, Zhu L, et al. Fabrication of adsorbents with thermocontrolled molecular gates for both selective adsorption and efficient regeneration. Adv Mater Interfaces 2016;3 (11):1500829.

[52] Jiang Y, Tan P, Cheng L, Shan SF, Liu XQ, Sun LB. Selective adsorption and efficient regeneration via smart adsorbents possessing thermo-controlled molecular switches. Phys Chem Chem Phys 2016;18(15):9883–7.

[53] Yin Y, Tan P, Liu XQ, Zhu J, Sun LB. Constructing a confined space in silica nanopores: an ideal platform for the formation and dispersion of cuprous sites. J Mater Chem A 2014;2(10):3399–406.

[54] Xing ZM, Gao YX, Shi LY, Liu XQ, Jiang Y, Sun LB. Fabrication of gold nanoparticles in confined spaces using solid-phase reduction: significant enhancement of dispersion degree and catalytic activity. Chem Eng Sci 2017;158:216–26.

[55] Yin Y, Zhu J, Liu XQ, Tan P, Xue DM, Xing ZM, et al. Simultaneous fabrication of bifunctional Cu(I)/Ce(IV) sites in silica nanopores using a guests-redox strategy. RSC Adv 2016;6(74):70446–51.

[56] Cho EB, Yim S, Kim D, Jaroniec M. Surfactant-assisted synthesis of mesoporous silica/ceria-silica composites with high cerium content under basic conditions. J Mater Chem A 2013;1(40):12595–605.

[57] Tan P, Li YH, Liu XQ, Jiang Y, Sun LB. Core-shell AgCl@SiO₂ nanoparticles: Ag(I)-based antibacterial materials with enhanced stability. ACS Sustain Chem Eng 2016;4(6):3268–75.

[58] Huang L, Xing ZM, Kou Y, Shi LY, Liu XQ, Jiang Y, et al. Fabrication of rhodium nanoparticles with reduced sizes: an exploration of confined spaces. Ind Eng Chem Res 2018;57(10):3561–6.

[59] Ho KY, McKay G, Yeung KL. Selective adsorbents from ordered mesoporous silica. Langmuir 2003;19(7):3019–24.

[60] Park SH, Kim BH, Selvaraj M, Lee TG. Synthesis and characterization of mesoporous Ce-Mn-MCM-41 molecular sieves. J Ind Eng Chem 2007;13 (4):637–43.

[61] Wang L, Wang J, He C, Lyu W, Zhang W, Yan W, et al. Development of rare earth element doped magnetic biochars with enhanced phosphate adsorption performance. Colloids Surf A 2019;561:236–43.

[62] Yang JM, Ying RJ, Han CX, Hu QT, Xu HM, Li JH, et al. Adsorptive removal of organic dyes from aqueous solution by a Zr-based metal–organic framework: effects of Ce(III) doping. Dalton Trans 2018;47(11):3913–20.

[63] Liu Y, Zeng G, Tang L, Cai Y, Pang Y, Zhang Y, et al. Highly effective adsorption of cationic and anionic dyes on magnetic Fe/Ni nanoparticles doped bimodal mesoporous carbon. J Colloid Interface Sci 2015;448:451–9.